A Hybrid Electromagnetic Model for Tubular Permanent Magnet Linear Synchronous Motors Based on Transfer Learning

Tao Wu, *Senior Member IEEE*, Gang Xue, Gang Lei, *Senior Member, IEEE,* Youguang Guo, *Senior Member, IEEE,* Jianguo Zhu, *Senior Member, IEEE*

Abstract—**Accurate electromagnetic modeling and analysis are crucial for the design optimization of tubular permanent magnet linear synchronous motors (TPMLSMs). This paper proposes a new electromagnetic modeling method for TPMLSMs based on transfer learning deep neural network (DNN). It integrates the electromagnetic mechanism into the data-driven model to achieve high-precision electromagnetic analysis with a small number of finite element analysis (FEA) samples. First, the electromagnetic analytical model of the slotted TPMLSM is derived from the motors' structural parameters and relative permeability function. Second, a hybrid model based on transfer learning is developed, which is pre-trained on a large dataset generated by the analytical model of the mechanism. The trained model is then optimized in the target field using a few high-precision FEA samples to improve the prediction accuracy of the hybrid model. Appropriate combinations of training FEA samples are selected based on sensitivity analysis to further improve the model's prediction accuracy and generalization ability. Third, experimental results demonstrate that the proposed method can significantly enhance the DNN model's performance, especially when training sets are small.**

Index Terms—**deep neural network, electromagnetic analytical model, hybrid electromagnetic model, data-driven method, tubular permanent magnet linear synchronous motors, sensitivity analysis, transfer learning.**

I. INTRODUCTION

Tubular permanent magnet linear synchronous motors (TPMLSMs) are widely used in refrigerators [1], computer numerical control (CNC) machine tools [2], air conditioning linear compressors [3], electromagnetic hammers [4], and other industrial applications because of their easy installation and small sizes. While the slotted core

T. Wu and G. Xue are with the School of Automation, China University of Geosciences, Wuhan 430074, China, and also with the Hubei Key Laboratory of Advanced Control and Intelligent Automation for Complex Systems, Wuhan 430074, China (e-mails: wutao@cug.edu.cn; 20191001356@cug.edu.cn).

Y. Guo and G. Lei are with the School of Electrical and Data Engineering, University of Technology Sydney, NSW 2007, Australia (e-mails: youguang.guo-1@uts.edu.au; gang.lei@uts.edu.au).

J. Zhu is with the School of Electrical and Computer Engineering, The University of Sydney, Sydney, NSW 2006, Australia (e-mail: jianguo.zhu@sydney.edu.au).

TPMLSMs offer high thrust density, accurately calculating the electromagnetic field distribution is a challenge due to the nonlinearity introduced by core saturation. An accurate and efficient electromagnetic calculation model is desirable for the optimal design of these motors [5].

At present, the commonly used electromagnetic analysis methods for TPMLSMs include the finite element method (FEM), equivalent magnetic circuit (EMC) method, and analytical method (AM). The FEM can solve complex transient problems and is well-suited for quantitative analysis and optimal design [6], but it has a high computational cost. The EMC method expresses the magnetic flux paths in the form of magnetic circuits [7,8]. A dynamic electromagnetic compatibility modeling and analysis method was proposed in [9]. However, this method only yields the average magnetic field distribution of the motor, making it suitable for qualitative analysis but insufficient for precise calculations.

The AM method formulates the control field equation based on Maxwell's equations and Lorentz force law, determining the motor's magnetic field distribution by solving the associated partial differential equations [10]. Common methods such as the relative permeability function method are based on the slotless analytical model, and the permeability function is calculated by introducing the Carter coefficient to consider the alveolar effect [11]. Although this method is concise, it cannot fully consider the tangential slot effect, and the calculation accuracy is limited. Conformal transformation method has high calculation accuracy, but it involves the mutual conversion between multiple complex planes, and the calculation process is extremely complicated [12]. The precise subdomain method, based on Fourier analysis, accounts for the motor's longitudinal edge effect by incorporating a sufficiently long arc region to include additional computational domains and higher harmonics [13]. However, this method has high computational costs, exhibits grid dependence, and performs poorly when handling complex boundary conditions and aperiodic problems.

Given the limitations of the aforementioned methods, data-driven approaches have been introduced for electromagnetic field analysis in motors. These methods excel in nonlinear fitting and are well-suited for motor optimization [14]. However, they require large datasets and are prone to overfitting when real-world data is insufficient.

Transfer learning can help solve the target task through the knowledge learned from the source task to achieve fast and efficient learning when solving similar problems [15,16]. This paper proposes a hybrid data-driven method that combines AM and FEM using transfer learning to enhance the prediction

performance of the data-driven model in cases where finite element data is insufficient. The experimental results show that the proposed method can significantly improve the model's prediction accuracy.

The main contributions of this paper are as follows:

1) Based on the motor structural parameters and relative permeability function, an analytical electromagnetic model is constructed for the TPMLSM, considering the backlash between the stator and the mover.

2) A data-driven modeling method based on deep neural network (DNN) is proposed, which uses Bayesian optimization to find the optimal hyperparameters and provides a convenient pre-trained model structure for transfer learning.

3) A hybrid modeling method based on transfer learning is proposed, which can significantly improve the performance of DNN on small sample training sets.

II. MOTOR STRUCTURE AND ELECTROMAGNETIC FIELD ANALYSIS OF THE TPMLSM

A. Motor Structure

Fig.1 illustrates the structure of the TPMLSM studied in this paper, consisting of three parts: the mover, air gap, and stator. The mover includes permanent magnets (PMs), pole shoes, and a secondary iron core. The stator includes a primary iron core and three-phase AC windings. The PMs are axially magnetized along the z-axis. Table I lists the main parameters of the TPMLSM.
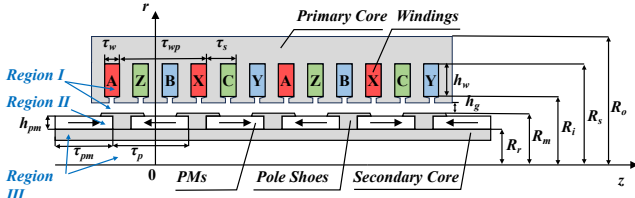

Fig. 1. Geometric structure of the TPMLSM.

TABLE I
MAIN DIMENSIONAL PARAMETERS OF THE TPMLSM

Name	Symbol	Value	Unit
Inner radius of PMs	R_r	8.5	mm
Outer radius of the mover	R_m	15.9	mm
Inner radius of the stator winding	R_i	17.9	mm
Outer radius of the stator winding	R_s	25.9	mm
Outer radius of the motor	R_o	33.4	mm
Mover pole pitch	τ_p	36	mm
Slot pitch	τ_s	12	mm
Axial length of one-phase coil	τ_w	8	mm
Winding pitch	τ_{wp}	36	mm
Current density	J_m	4	A/mm²
Axial length of PMs	τ_{pm}	28.8	mm
Thickness of PMs	h_{pm}	6	mm
Thickness of air gap	h_g	1	mm
Thickness of coils	h_w	8	mm
Slot opening width	b_0	2.4	mm

B. Analytical Electromagnetic Model

An analytical electromagnetic model is developed for the slotted TPMLSM studied in this paper, assuming an infinite axial length, i.e., an axially symmetric and periodic field distribution along the z-axis, and utilizing the Carter coefficient or the relative permeability function to account for

the tooth-slot effect on the stator winding side [5]. During the magnetic field analysis, the permeability of Regions I (the winding and airgap) and III (the secondary core made of non-ferromagnetic stainless steel) is assigned as μ_0 and Region II (the PMs) $\mu_0\mu_r$, where μ_r is the relative permeability of PMs. Since the field is radially and axially symmetric, the governing field equation can be expressed in the tangential component of the vectorial magnetic potential, A_θ, as follows:

$$\begin{cases} \frac{\partial}{\partial z}\left(\frac{1}{r}\frac{\partial}{\partial z}(rA_{I,III\theta})\right) + \frac{\partial}{\partial r}\left(\frac{1}{r}\frac{\partial}{\partial r}(rA_{I,III\theta})\right) = 0 \\ \frac{\partial}{\partial z}\left(\frac{1}{r}\frac{\partial}{\partial z}(rA_{II\theta})\right) + \frac{\partial}{\partial r}\left(\frac{1}{r}\frac{\partial}{\partial r}(rA_{II\theta})\right) = -\mu_0\nabla\times M \end{cases} \quad (1)$$

where $A_{I,III\theta}$ is the tangential component of the vectorial magnetic potential of Regions I and III, and $A_{II\theta}$ the tangential component of the vectorial magnetic of Region II.

The magnetization vector of the PMs can be expressed as:

$$\boldsymbol{M} = M_z \boldsymbol{e}_z \quad (2)$$

where M_z is the axial magnetization component, which can be expanded into a Fourier series as follows.

$$M_z = \sum_{n=1,2\ldots}^{\infty} \frac{4B_r}{\mu_0(2n-1)\pi}\sin\left(\frac{(2n-1)\pi\alpha_p}{2}\right)\cos m_n z \quad (3)$$

where B_r is the remanence of the PMs, and m_n and α_p are defined as:

$$\begin{cases} m_n = \frac{(2n-1)\pi}{\tau_p} \\ \alpha_p = \frac{\tau_{pm}}{\tau_p} \end{cases} \quad (4)$$

The governing field equation of the TMPLSM will be solved together with the boundary conditions defined as follows:

$$\begin{cases} B_{I_z}|_{r=R_s} = 0, B_{III_r}|_{r=0} = 0 \\ B_{I_z}|_{z=\tau_p/2} = 0, B_{I_r}|_{z=0} = 0 \\ B_{I_z}|_{\tau_{pm}/2<z<\tau_p/2}^{r=R_m} = 0, B_{III_z}|_{\tau_{pm}/2<z<\tau_p/2}^{r=R_r} = 0 \\ B_{II_r}|_{z=\tau_{pm}/2} = 0 \\ B_{I_z}|_{0\le z\le\tau_{pm}/2}^{r=R_m} = B_{II_r}|_{0\le z\le\tau_{pm}/2}^{r=R_m} \\ H_{I_z}|_{0\le z<\tau_{pm}/2}^{r=R_m} = H_{II_r}|_{0\le z\le\tau_{pm}/2}^{r=R_m} \\ B_{II_r}|_{0\le z\le\tau_{pm}/2}^{r=R_r} = B_{III_r}|_{0\le z\le\tau_{pm}/2}^{r=R_r} \\ H_{II_r}|_{0\le z\le\tau_{pm}/2}^{r=R_r} = H_{III_r}|_{0\le z\le\tau_{pm}/2}^{r=R_r} \\ \int_{R_r}^{R_m} rB_{II_z}(r,\frac{\tau_{pm}}{2})dr = \int_{\tau_{pm}/2}^{\tau_p/2}[R_m B_{I_r}(R_m,Z) \\ \qquad\qquad\qquad -R_r B_{III_r}(R_r,Z)]dZ \end{cases} \quad (5)$$

where B_{I_z} and H_{I_z} are the z components of magnetic flux density and field strength in Region I, respectively.

Solving the field problem defined by the governing equations (1)-(4) and boundary condition (5), one obtains the TPMLSM's slot-less air gap magnetic field distribution as follows.

$$\begin{cases} B_{Ir}(r,z) = \sum_{n=1}^{\infty}[a_{In}BI_1(m_n r) \\ \qquad\qquad +b_{In}BK_1(m_n r)]\sin m_n z \\ B_{Ir}(r,z) = \sum_{n=1}^{\infty}[a_{In}BI_0(m_n r) \\ \qquad\qquad -b_{In}BK_0(m_n r)]\sin m_n z \end{cases} \quad (6)$$

where $BI_0(\bullet)$ and $BI_1(\bullet)$ are the modified Bessel functions of the first kind, $BK_0(\bullet)$ and $BK_1(\bullet)$ are the modified Bessel functions of the second kind, and a_{In} and b_{In} are the (2n-

1)*th* subharmonic coefficients related to axial magnetization in the air gap region, depending on the material characteristics and geometric parameters of PMs [17].

Therefore, assuming that the TPMLSM stator has no slot, the radial and axial components of the air gap magnetic flux density at $r = R_m + h_g/2$ can be obtained by using the AM. Figs. 2 and 3 compare the AM and FEM results for the radial and axial air gap flux densities, respectively. As shown, the results of both methods are in good agreement with the overall trend in the slotless TPMLSM. Without the influence of tooth gap, the AM is relatively accurate.
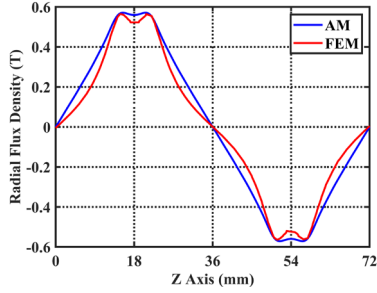

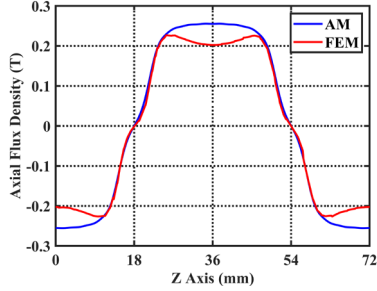**Fig. 2.** Radial air gap flux density of the slotless TPMLSM.

Fig. 3. Axial air gap flux density of the slotless TPMLSM.

If the armature winding is of finite length and is slotted, the cogging effect on the air gap flux density can be interpreted by introducing the Carter coefficient [18].

$$K_c = \frac{\tau_s}{\tau_s - \gamma h_g'} \tag{7}$$

where γ, the notch coefficient, can be expressed as

$$\begin{cases} \gamma = \frac{4}{\pi}\left(\frac{b_0}{2h_g'}arctan(\frac{b_0}{2h_g'}) - ln\sqrt{1 + (\frac{b_0}{2h_g'})^2}\right) \\ h_g' = h_g + \frac{h_{pm}}{\mu_r} \end{cases} \tag{8}$$

To accurately represent the air gap flux density distribution, the motor's air gap permeability function at the specific spatial location of a single slot is considered, which can be expressed as:

$$\lambda(r,z) = \begin{cases} \Lambda_0[1 - \beta(r)(1 + cos\frac{z}{0.8z_0}\pi)], 0 \leq z \leq 0.8b_0 \\ \Lambda_0, 0.8b_0 \leq z \leq \tau_s \end{cases} \tag{9}$$

and $\beta(r)$ is defined as:

$$\beta(r) = \frac{1}{2} - \frac{1/2}{\sqrt{1 - \left(\frac{b_0}{2h_g'}\right)^2(1+v^2)}} \tag{10}$$

where z_0 is a feature-length parameter in the z-direction, $\Lambda_0 = \mu_0/h_g'$, and $g_c = K_c h_g$; v is the solution of the following equation:

$$y\frac{\pi}{b_0} = \frac{1}{2}ln\left(\frac{\sqrt{a^2+v^2}}{\sqrt{a^2+v^2}-v}\right) + \frac{2h_g'}{b_0}arctan\left(\frac{2h_g'}{b_0}\frac{v}{\sqrt{a^2+v^2}}\right) \tag{11}$$

where

$$\begin{cases} a = \sqrt{1 + \left(\frac{2h_g'}{b_0}\right)^2} \\ y = r - (R_s - h_g - h_{pm}) \end{cases} \tag{12}$$

Thus, the spatial distribution of the slotted TPMLSM air gap flux density can be obtained as:

$$\begin{cases} \hat{B}_r(r,z) = \tilde{\lambda}(r,z)B_r(r,z) \\ \hat{B}_z(r,z) = \tilde{\lambda}(r,z)B_z(r,z) \end{cases} \tag{13}$$

where

$$\tilde{\lambda}(r,z) = \frac{\lambda(r,z)}{\Lambda_0} \tag{14}$$

Figs. 4 and 5 compare the AM and FEM results of the radial and axial air gap flux densities of the slotted TPMLSM, respectively. Compared with the slotless case, there is a large deviation between the AM and FEM results of the slotted case, indicating that the spatial magnetic field distribution of the slotted TPMLSM cannot be accurately calculated by using the relative permeability function and the Carter coefficient.
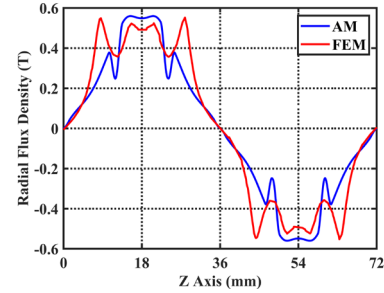

Fig. 4. Radial air gap flux density of the slotted TPMLSM.
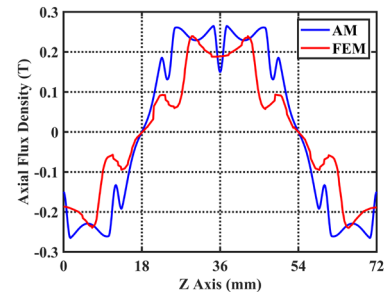
Fig. 5. Axial air gap flux density of the slotted TPMLSM.

From Figs. 4 and 5, it can be seen that the magnetic field distribution becomes more complex in the slotted TPMLSM due to the existence of the slot structure. The Carter coefficient can basically reflect the influence of tooth and slot on air gap magnetic density, but the error becomes larger compared with FEM.

Once the slotted air gap magnetic field is calculated, the motor thrust and coil copper losses can be deduced. The TPMLSM's thrust is generated by the interaction between the winding current and the PM field and can be calculated by

$$F = \int_V (J \times B) dV \tag{15}$$

where J is the current density, and B the magnetic flux density.

The total thrust force generated by a phase winding of multiple coils can be expressed as:

$$F = -\int_{z-\tau_w/2}^{z+\tau_w/2} \int_{R_i}^{R_s} 2\pi r J B_r(r, z) dr dz \tag{16}$$

Assuming full pitch winding, i.e., $\tau_s = \tau_{wp}$, the three-phase windings are distributed by 2/3 pole-pitches apart, and there is one coil per pole per phase, and then the current density of each phase winding can be expressed as:

$$\begin{cases} J_A = \sqrt{2} J_m \sin(\omega t) \\ J_B = \sqrt{2} J_m \sin(\omega t - 2\pi/3) \\ J_C = \sqrt{2} J_m \sin(\omega t + 2\pi/3) \end{cases} \tag{17}$$

where J_m is the magnitude of current density, and $\omega = \pi z / \tau_p$ is the current angular frequency.

If the mover runs at a uniform linear velocity, $v = 2\tau f$, the total instantaneous thrust can be expressed as:

$$\begin{aligned} F &= F_A + F_B + F_C \\ &= \sqrt{2} J_m \sum_{n=1}^{\infty} K_{T_n} \Big[\cos\big(m_n(z - \tau_p/2)\big) \sin(\omega t) \\ &\quad + \cos\big(m_n(z - 7\tau_p/6)\big) \sin(\omega t - 2\pi/3) \\ &\quad + \cos\big(m_n(z + \tau_p/6)\big) \sin(\omega t + 2\pi/3) \Big] \end{aligned} \tag{18}$$

where m_n is the spatial wave number of the nth harmonic, and K_{Tn} is the thrust constant expressed as:

$$K_{Tn} = -4\pi K_{dpn} \left\{ \frac{\mu_0 H_{pm} h_{pm} \sin(m_n h_{pm}/2)}{m_n \tau_p (R_s - R_{ie}) \Delta_1} \right\} \int_{R_{ie}}^{R_s} r \Delta_3(r) dr \tag{19}$$

The equivalent air gap h_{ge} and the equivalent armature radius R_{ie} are given as:

$$\begin{cases} h_{ge} = h_g + (K_c - 1) h_g' \\ R_{ie} = R_m + h_{ge} \end{cases} \tag{20}$$

and Δ_1 and $\Delta_3(r)$ can be expressed by the Bessel function as:

$$\begin{cases} \Delta_1 = BI_0(m_n R_s) BK_0(m R_m) - BI_0(m_n R_m) BK_0(m R_s) \\ \Delta_3(r) = BI_0(m_n R_s) BK_1(m r) - BI_1(m_n r) BK_0(m R_s) \end{cases} \tag{21}$$

Assuming that the PM is uniformly magnetized, the average working magnetic field strength can be regarded as the working point of the PM [19], as shown in Fig. 6.
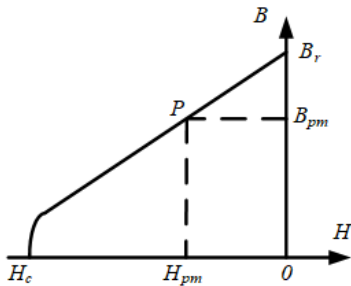

Fig. 6. Demagnetization curves and operating points of PMs.

The magnetic field strength at P can be calculated by:

$$H_{pm} = \frac{B_r - B_{pm}}{\mu_0 \mu_r} \tag{22}$$

where B_{pm} is the magnetic flux density at the operating point.

In addition, K_{dpn}, the winding pitch coefficient K_{pn}, and the (2n-1)th harmonic winding distribution coefficient K_{dn} are expressed as:

$$\begin{cases} K_{dpn} = K_{pn} K_{dn} \\ K_{pn} = \sin(m_n \tau_s/2) \\ K_{dn} = \sin(m_n \tau_w/2)/(m_n \tau_w/2) \end{cases} \tag{23}$$

Therefore, the average thrust and thrust fluctuation when the motor moves linearly for a distance can be obtained by:

$$\begin{cases} F_{av} = \frac{1}{s} \sum_{z=0}^{s} F(z) \\ F_{pk} = max(F(z)) - min(F(z)) \end{cases} \tag{24}$$

Assuming that the stator slot fill factor K_w equals 0.8, one obtains the winding current effective value as:

$$i = J_m S_d \tag{25}$$

where $S_d = \tau_w h_w K_w / N_{wp}$ is the cross-sectional area of the enameled wire and N_{wp} is the number of turns of the coil.

The coil copper loss of the three-phase winding during the whole movement can be expressed as:

$$P_{cua} = 3i^2 R = 3(J_m S_d)^2 R \tag{26}$$

where the phase winding resistance can be expressed as:

$$R = 2\pi N_{wp}(R_i + (R_s - R_i)/N_{wp})/S_d \tag{27}$$

III. DATA-DRIVEN HYBRID MODELING METHOD

A. TPMLSM Electromagnetic Field Dataset

To obtain the electromagnetic field datasets of the TPMLSM, five geometrical parameters in Table I are selected as independent variables. Their variation ranges and steps are listed in Table II. According to the settings in Table II, 1440 sets of electromagnetic field data are calculated using finite element analysis (FEA) with these five geometric parameters as inputs, and the average thrust, thrust fluctuation, and average coil copper loss are the outputs. It should be noted that although 1440 sets of FEA data are used for model training or validation, it does not mean that such a large amount of data is required in practical applications.

TABLE II
SETTING OF TPMLSM INDEPENDENT VARIABLES

Variables	Default Value	Variation Range	Variation Step	Unit
τ_{pm}	28.8	18-28.8	3.6	mm
h_{pm}	6	4.8-6.8	0.4	mm
h_g	1	0.8-1.4	0.2	mm
h_w	8	8-10	1	mm
b_0	2.4	2.2-3	0.2	mm

B. DNN Model Structure

Due to the limited accuracy of the electromagnetic AM, there are significant deviations between the predicted results and the actual performance parameters. Thus, this paper uses DNN to construct a data-driven model for the TPMLSM. The DNN is a multi-hidden-layer neural network that can learn complex features and representations efficiently and is suitable for fitting complex nonlinear mapping of motors' electromagnetic fields. The DNN model selected here is a lightweight model, which contains an input layer, four hidden layers, and an output layer. Among them, the input layer has

five neurons, corresponding to the five motor parameters (τ_{pm}, h_{pm}, b_0, h_g, h_w). The neuron numbers in the four hidden layers are 16, 8, 8, and 8, respectively; and the output layer consists of three neurons, corresponding to the three performance indexes, i.e., average thrust, thrust fluctuation, and average coil copper loss. Fig. 7 illustrates the input layer, multiple hidden layers, and output layer of such a DNN model. The number of neurons in the input and output layers depends on the dataset dimension, while the hidden layer structure is regarded as a hyperparameter, which is determined by experience or optimization algorithms with the activation function, learning rate, and training period. The EM model of slotted TPMLSM is not so complex, so this light DNN model is suitable here, which avoids over-computation and excessive demand for training samples.
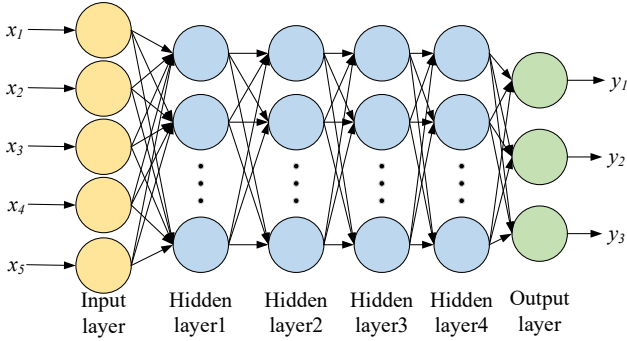

Fig. 7. Structure diagram of DNN model.

To obtain the optimal combination of hyperparameters, this paper adopts the Bayesian optimization algorithm in MATLAB to optimize DNN hyperparameters [20]. The maximum number of iterations is set to 6. The setting of the hyperparameters to be optimized is shown in Table III. The initial sampling points of each hyperparameter are set as follows: the activation function as ReLU, the optimization algorithm as Adam, the number of hidden layers as 2, the number of neurons in each layer as 10, and the initial learning rate as 0.001. The maximum training period of DNN is set as 70, and the batch sample size is 50. The linear attenuation function of epochs with an attenuation coefficient of 0.2 and a period of 10 is used to update the learning rate automatically during the training.

TABLE III
TO-BE-OPTIMIZED HYPERPARAMETER SETTINGS IN DNN

Hyperparameter name	Optimization Scope
Activation function	[Sigmoid, Tanh, ReLU]
Optimization algorithm	[Adam, SGD, RMSprop, L-BFGS]
Number of hidden layers	1~5
Number of neurons in each hidden layer	1-300
Initial learning rate	$10^{-6} \sim 10^{-2}$

C. Data-Driven Hybrid Modeling

Fig. 8 shows a flowchart for the proposed data-driven hybrid modeling method for the TPMLSM.

Firstly, the AM dataset is preprocessed to form a source domain sample set A, and it is divided into a training set and a verification set. The FEM dataset is also preprocessed to obtain the target domain sample set B. The training set A is brought into the source domain, the data-driven model is pre-trained, and the hyperparameter adjustment is completed by validation set A combined with the Bayesian optimization algorithm. Secondly, based on the discrete sensitivity analysis of input features, specific samples are selected from the FEM dataset to form training set B, and the remaining data is used as test set B. The data-driven model with the best hyperparameters is transferred from the pre-trained output to training set B, that is, the weights and biases of the first few hidden layers of the fixed DNN model, after parameter fine-tuning and secondary training. It will be updated based on the characteristics of training set B in the team's top parameters. Finally, test set B is used to validate the post-migration model, compare the predicted performance with the real performance, and calculate the evaluation metrics.
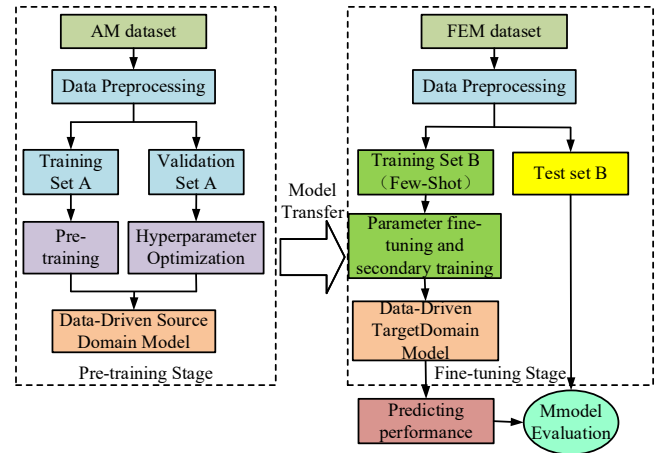

Fig. 8. TPMLSM data-driven hybrid modeling process.

D. Model Evaluation

To verify the accuracy of the data-driven model, the root mean square error (RMSE), mean absolute error (MAE), correlation coefficient (R^2), median absolute error (MEDAE), and mean absolute percentage error (MAPE) are selected as evaluation criteria to assess the model's training accuracy and generalization performance.

RMSE is defined as follows to measure the standard deviation of the error between the actual and predicted values of the model.

$$RMSE = \sqrt{\frac{1}{nm}\sum_{i=1}^{n}\sum_{j=1}^{m}(y_{ij} - \hat{y}_{ij})^2} \qquad (28)$$

MAE is defined as follows to measure the non-bias of the model and is less sensitive to errors than RMSE.

$$MAE = \frac{1}{nm}\sum_{i=1}^{n}\sum_{j=1}^{m}|y_{ij} - \hat{y}_{ij}| \qquad (29)$$

R^2 is defined as follows to evaluate the fitting degree of the model to the true value.

$$R^2 = 1 - \frac{\sum_{i=1}^{n}\sum_{j=1}^{m}(y_{ij} - \hat{y}_{ij})^2}{\sum_{i=1}^{n}\sum_{j=1}^{m}(y_{ij} - \bar{y}_j)^2} \qquad (30)$$

MEDAE is the median prediction error,

$$MEDAE = \frac{1}{m}\sum_{j=1}^{m} median\left(|y_{ij} - \hat{y}_{ij}|\right) \qquad (31)$$

It is used to measure the deviation between the predicted values of the model and the actual values.

MAPE is a measure of the relative error between the predicted and actual values of the model and is defined as:

$$MAPE = \frac{1}{m}\sum_{j=1}^{m}(\frac{1}{n}\sum_{i=1}^{n}|\frac{y_{ij}-\hat{y}_{ij}}{y_{ij}}|) \qquad (32)$$

where n denotes the number of samples in the FEA dataset, m the number of labels, $\bar{y}_j$ the average value of the jth label, and $\hat{y}_{ij}$ and y_{ij} are the predicted and true values of the jth label of the ith sample, respectively.

The above formula serves as an evaluation index for a single output. The larger the R² value and the smaller the values of other indicators, the better the model's predictive performance. The model of this paper is a five-input and three-output model, and the final evaluation index is calculated by averaging the single index of the three outputs. Taking RMSE as an example, it can be calculated as follows:

$$RMSE_{avg} = \frac{1}{3}(RMSE_{average\ thrust} + RMSE_{thrust\ fluctuation}$$
$$+RMSE_{copper\ loss}) \qquad (33)$$

where $RMSE_{average\ thrust}$, $RMSE_{thrust\ fluctuation}$, and $RMSE_{copper\ loss}$ are the RMSE indexes of the average thrust, thrust fluctuation, and average coil copper loss, respectively. By averaging the three separate RMSE values, the comprehensive RMSE evaluation index of the model can be obtained. Here, we adopt the simple arithmetic mean of the three metrics as an overall performance indicator. In practice, the relative importance of each output may differ by application. Therefore, users can adjust the weighting of individual metrics to obtain a more tailored evaluation.

IV. RESULTS AND DISCUSSION

A. Pre-training

The purpose of the pre-training is to obtain a data-driven model that fits the AM dataset to describe as many of the data properties of the TPMLSM electromagnetic field as possible. Ninety percent of the AM dataset is used for pre-training of the DNN, random forest (RF), and support vector machine (SVM), with the remaining 10% reserved for validation. Ten-fold cross-validation is used to calculate the model evaluation indexes of each data-driven model on the verification set after pre-training. As shown in Table IV, the DNN has the best fitting effect on electromagnetic mechanism data, and all evaluations are better than those of RF and SVM.

TABLE IV
PRE-TRAINED MODEL EVALUATION

	R²	MEADE	MAE	RMSE	MAPE
DNN	**0.9989**	**0.621**	**0.861**	**1.232**	**1.817**
RF	0.8130	4.845	5.649	9.189	8.713
SVM	0.8912	2.695	3.843	7.685	4.832

B. DNN and AM

TABLE V
PERFORMANCE EVALUATION OF DATA-DRIVEN MODELS (DNN)

Proportion of training data	R²	MEADE	MAE	RMSE	MAPE
5%	0.9393	3.535	5.482	7.834	13.371
10%	0.9777	2.418	3.429	4.719	8.149
20%	0.9812	2.199	3.148	4.336	7.486
50%	**0.9889**	**1.291**	**2.274**	**3.354**	**4.741**

To verify the DNN model's performance in fitting electromagnetic mechanism data, the FEM data set is randomly divided into training and test sets with ratios of 5:95, 1:9, 2:8, and 5:5. The model parameters are trained and adjusted in the target domain. Table V lists the performance indices.

As shown in Table V, the DNN model's predictive performance decreases in proportion to the decrease in the training data. When the proportion is reduced from 10% to 5%, the R² of the DNN model decreases from 0.9777 to 0.9393, and other error indicators increase significantly, indicating that the DNN model struggles to maintain excellent performance when the data is insufficient.

The AM can provide better reference data for model pre-training by describing the physical characteristics of the motor, which is helpful in optimizing the model performance. To evaluate the AM's performance, the AM dataset is compared with the FEM dataset. The AM has the best prediction of average coil copper loss, whose R² is 0.9547 and MAPE is only 2.0273, but the prediction of the average thrust and thrust fluctuation is poor, especially the average thrust, whose R² is -1.1245 and MAPE is as high as 21.3561. The overall index R² of AM is only 0.1117, indicating that AM has a poor prediction ability for the motor mechanism data. In contrast, the DNN model still has better prediction performance when the data is limited. To clearly show the accuracy between the AM and FEM, the deviation comparison of the two methods is demonstrated in Fig. 9.
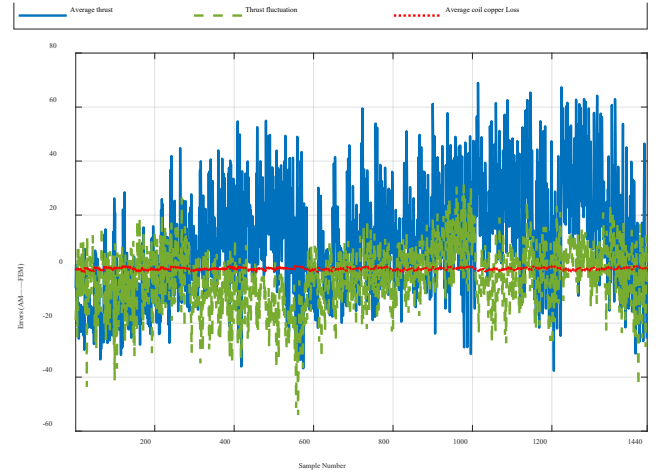

Fig. 9. Comparison of the deviation of the output results of the AM and FEM models plots.

C. Transfer Learning DNN (TL-DNN)

To verify the improvement of transfer learning on DNN models, the FEM data set is randomly divided into training sets and test sets in ratios of 5:95, 1:9, and 2:8. The pre-trained DNN model is retrained, and the parameters are adjusted in the target domain. Table VI lists the performance indicators.

As shown in Table VI, the TL-DNN model still shows excellent performance when the training data sample is small. With only 5% of the training data, R² of the TL-DNN and MAPE models reach 0.9882 and 6.487, respectively, which is significantly better than the performance of the DNN model when the training data is less than 20% of the total. The results

demonstrate that the transfer learning algorithm can significantly enhance the DNN model's prediction accuracy and stability, reducing its dependence on a large amount of training data.

TABLE VI
PERFORMANCE EVALUATION OF DATA-DRIVEN MODELS (TL-DNN)

Proportion of training data	R^2	MEADE	MAE	RMSE	MAPE
5%	0.9882	1.905	2.563	3.454	6.487
10%	0.9883	1.896	2.539	3.435	6.413
20%	**0.9894**	**1.878**	**2.455**	**3.271**	**6.161**

D. Sensitivity Analysis and Sample Selection

The relationship between the input features and the model's output results is discussed through discrete sensitivity analysis, allowing the influence of each feature on the model's performance to be quantified. Firstly, normalization and other pre-processing are carried out to identify the discrete values of each input feature and calculate the initial model output. Then, the discrete values of the features are replaced one by one to generate the corresponding model output. Finally, the output difference of the model before and after the disturbance is compared, the feature sensitivity value is calculated, and the key variables are accurately evaluated.

The discrete sensitivity value is calculated as follows:

$$S_i = \frac{1}{N}\sum_{k=1}^{N}|\hat{y}_i(x_k) - y(x_k)| \qquad (34)$$

where S_i is the sensitivity value of the ith input feature, N the sample size, $\hat{y}_i(x_k)$ the model output of the kth sample after perturbing the ith input feature, and $y(x_k)$ the model output of the kth sample under the original input feature.

Table VII lists the results of the discrete sensitivity analysis. As shown, τ_{pm} and h_{pm} have a significant impact on the output results of the model. b_0 has a relatively small effect on the model output; and h_g and h_w have the least impact on the model.

TABLE VII
DISCRETE SENSITIVITY ANALYSIS OF INPUT FEATURES

parameter	Average Thrust (N)	THRUST FLUCTUATION (N)	AVERAGE COIL COPPER LOSS (W)
τ_{pm}	17.917	8.697	0.642
h_{pm}	**18.626**	**8.816**	**0.662**
h_g	11.047	4.714	0.337
h_w	9.536	3.953	0.288
b_0	14.301	6.129	0.448

Based on the above analysis, before training the transfer learning model, the representative data should be selected as the training set according to the sensitivity results of the input features, and the rest is the test set. Features with high sensitivity should account for a large proportion of the training set to avoid random division. The specific sample selection is shown in Table VIII.

E. TL-DNN-Picking

To verify the enhancement effect of sample selection based on sensitivity analysis on the TL-DNN model, the FEM data set is divided into the training set and the test set according to

the selection shown in Table VIII. The pre-trained DNN model is retrained in the target domain, and the parameters are adjusted. The performance evaluation indicators are shown in Table IX.

TABLE VIII
SPECIFIC SAMPLE SELECTION

	100%	5%	10%	20%
τ_{pm}	4	3	3	3
h_{pm}	6	4	6	6
h_g	4	1	2	2
h_w	3	2	2	2
b_0	5	3	2	4
Total number	1440	72	144	288

TABLE IX
PERFORMANCE EVALUATION OF DATA-DRIVEN MODELS (TL-DNN-PICKING)

Proportion of training data	R^2	MEADE	MAE	RMSE	MAPE
5%	0.9875	1.311	2.399	3.575	5.245
10%	0.9887	1.284	2.296	3.428	5.137
20%	**0.9904**	**1.251**	**2.118**	**3.096**	**4.857**

As shown in Table IX, with the same proportion of training data, the performance of the TL-DNN-Picking model is significantly improved compared with that of the TL-DNN model. Taking 5% training data as an example, the MAPE of the TL-DNN-Picking model decreases from 6.487 to 5.245, and MEADE decreases from 1.905 to 1.311. The sample-picking strategy based on sensitivity analysis effectively enhances the predictive performance and accuracy of the TL-DNN model.

G. Prediction Performance Comparison of DNN, TL-DNN, TL-DNN-Picking Models

Fig. 10 compares the prediction performance of the DNN, TL-DNN, and TL-DNN-Picking models with different training set proportions. The quantization standard of MEADE, MAE, RMSE, and MAPE is based on the scale on the left Y-axis. The quantization standard of R^2 is based on the scale on the right Y-axis.
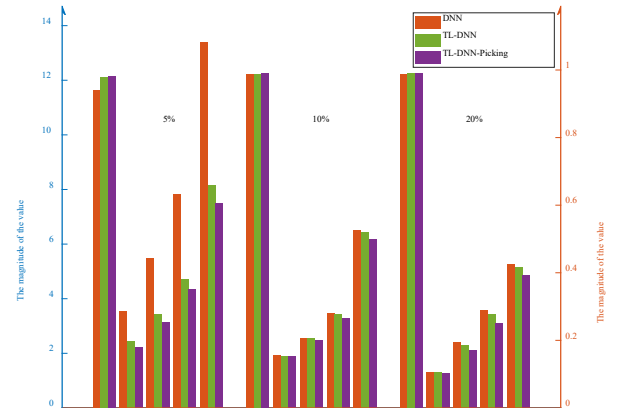

Fig. 10. Comparison diagram of model prediction performance evaluation.

As shown in Fig. 9, the TL-DNN model has been significantly improved compared to the DNN model in various performance indicators, verifying the effectiveness of transfer learning. Compared with the TL-DNN model, the TL-DNN-Picking model optimizes the sample selection through sensitivity analysis, further improving the performance. In summary, sample selection combined with transfer learning and sensitivity analysis can effectively improve the prediction accuracy of DNN models.

Regarding computational time, the FEM model takes approximately 20-30 minutes per calculation, and 1440 datasets cost nearly 480-720 hours. The AM model takes nearly 2-5 minutes, but the accuracy is the lowest. The operational complexity of the hybrid model is the highest because it only needs to acquire a small FEM dataset (a 5% training set, approximately 24 hours) and a pre-training time. The pre-training time of TL-DNN is about 2-4 hours (according to the data generated by AM model), a second-round training by FEM datasets is relatively fast about 2-4 minutes. Although the process of TL-DNN is complex, the output time of trained TL-DNN is quite fast, only requiring 0.5-3 seconds to output results, which is very suitable for optimization calculation.

V. EXPERIMENT AND COMPARISON

To validate the accuracy of the TL-DNN model, a prototype of TPMLSM has been built and tested, as shown in Fig. 11.

Fig. 11. Physical diagram of the test platform.

Table X compares the thrust and copper loss under different phase currents predicted by the TL-DNN-Picking model and FEM, and the experimental results. As shown, the thrust error between the TL-DNN-Picking predictions and experimental measurements is less than 3%, and the copper loss error is less than 2% at higher currents.

TABLE X
COMPARISON OF THRUST AND COPPER LOSS PREDICTED WITH DIFFERENT PHASE CURRENTS

Phase Current (A)	Thrust Experiment (N)	Thrust FEM (N)	Thrust TL-DNN (N)	Copper Loss Experiment (W)	Copper Loss AM (W)	Copper Loss TL-DNN (W)
0.5	49.23	49.72	50.31	8.23	6.75	6.78
1.0	98.80	99.78	101.68	28.40	27.00	27.50
1.5	151.41	153.18	154.56	61.52	60.75	60.95
2.0	203.09	205.14	207.43	109.20	108.00	108.98
2.5	247.35	250.36	253.13	169.50	168.75	169.01
3.0	297.77	300.54	304.52	243.90	243.00	243.70
3.5	348.21	353.74	357.73	331.15	330.75	330.90

The peak value of the single-phase current waveform in the two-dimensional FEA is 1.24 A, which is close to the experimentally measured peak value of 1.22 A under the condition of 3.6 m/s, as shown in Fig. 12. Due to the limitation that the structural dimensions of the prototype have been determined, there is only limited experimental data to support this. As the TL-DNN model is trained by FEM data and is very similar to the FEM, it only needs to verify the accuracy between the FEM and the actual prototype. Furthermore, if there is enough experimental data, the TL-DNN model can be trained to compensate for the difference between the predicted values and the actual motor.
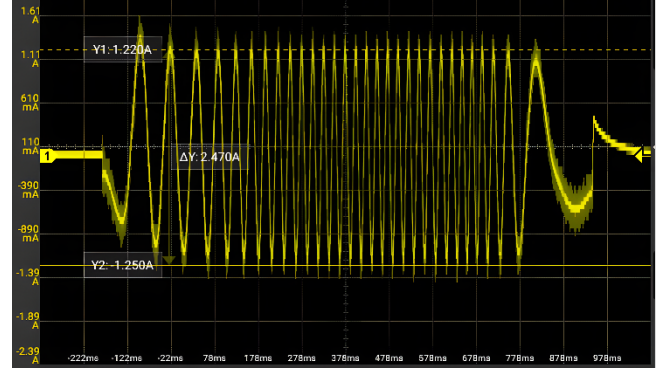

Fig. 12. TPMLSM single-phase current waveform measurement.

VI. CONCLUSION

This paper proposed a hybrid modeling method of electromagnetic fields in TPMLSMs, which combines the electromagnetic mechanism model with the FEA data into a DNN model to achieve high-precision electromagnetic field analysis with a small number of FEA samples. Based on transfer learning, the AM data set was used to pre-train the DNN model, and the FEA data set was used to optimize the pre-trained DNN model in the target domain, which improves the prediction performance of the DNN model. The training data was selected based on sensitivity analysis, which can further improve the predictive performance of the TL-DNN model and reduce the need for finite element sample quantity in the process of motor optimization. The effectiveness of the proposed method was verified by experimental tests on a prototype. Compared with the existing methods, the proposed model has better performance with a small training data set.

In the future, with the addition of more experimental data, the hybrid model can further improve the accuracy of the model, rather than relying only on the FEA data. Furthermore, a more accurate electromagnetic and temperature coupling field hybrid model can be jointly established using the AM, equivalent thermal path method, FEA, and data-driven modeling methods, to improve the overall motor performance.

REFERENCES

[1] W. Xu, *et al.*, "Improved adaptive terminal sliding-mode reaching law for speed control of TPMLSM with disturbance observer," *IEEE Transactions on Industry Applications*, vol. 59, no. 3, pp. 3210-3219, May-June 2023.

[2] K. Erwinski, A. Wawrzak, and M. Paprocki, "Real-time jerk limited feedrate profiling and interpolation for linear motor multiaxis machines

using NURBS toolpaths," *IEEE Transactions on Industrial Informatics*, vol. 18, no. 11, pp. 7560-7571, Nov. 2022.

[3] J. Chen, Y. Fan, Q. Zhang, Q. Chen, and M. Cheng, "Ultralocal model-based tuning-free controller for PMSM drives considering control frequency," *IEEE Transactions on Industrial Electronics*, vol. 71, no. 8, pp. 9956-9961, Aug. 2024.

[4] S. Wu, C. Hu, Z. Zhao, and Y. Zhu, "High-accuracy sensorless control of permanent magnet linear synchronous motors for variable speed trajectories," *IEEE Transactions on Industrial Electronics*, vol. 71, no. 5, pp. 4396-4406, May 2024.

[5] Q. Tan, X. Huang, L. Li, and M. Wang, "Analysis of flux linkage and detent force for a modular tubular permanent magnet synchronous linear motor with large slots," *IEEE Transactions on Energy Conversion*, vol. 34, no. 3, pp. 1532–1541, 2019.

[6] G. Lv, L. Cui, and R. Zhi, "Inductance analysis of transverse flux linear synchronous motor for maglev trains considering three-dimensional operating conditions," *IEEE Transactions on Industrial Electronics*, vol. 71, no. 1, pp. 769-776, Jan. 2024.

[7] Z. Zhang, M. Luo, J. -A. Duan, and B. Kou, "Performance analysis of double-sided permanent magnet linear synchronous motor with quasi-sinusoidal ring windings," *IEEE Transactions on Energy Conversion*, vol. 35, no. 3, pp. 1465-1474, Sept. 2020.

[8] Y. Du, *et al.*, "Equivalent magnetic circuit analysis of doubly salient PM machine with Π-shaped stator iron core segments," *IEEE Transactions on Applied Superconductivity*, vol. 30, no. 4, pp. 1-5, June 2020, Art no. 5201505.

[9] G. Yu, Y. Xu, T. Lin, L. Xiao, J. Zou, and J. Tan, "Nonlinear EMC modeling and analysis of permanent-magnet slotted limited-angle torque motor," *IEEE Transactions on Industrial Electronics*, vol. 68, no. 9, pp. 8507-8518, Sept. 2021.

[10] H. Hua and W. Hua, "Analytical prediction of torque of switched reluctance machines considering nonlinear characteristics," *IEEE Transactions on Industrial Electronics*, vol. 69, no. 1, pp. 190-201, Jan. 2022.

[11] Y. Zhou, R. Qu, C. Shi, and Y. Gao, "Analysis of thrust performance of a dual-mover linear vernier machine with horizontal-magnetized PM arrays," *IEEE Transactions on Energy Conversion*, vol. 33, no. 4, pp. 2143–2152, 2018.

[12] Q. Lu, B. Wu, Y. Yao, Y. Shen, and Q. Jiang, "Analytical model of permanent magnet linear synchronous machines considering end effect and slotting effect," *IEEE Transactions on Energy Conversion*, vol. 35, no. 1, pp. 139-148, Mar. 2020.

[13] Y. Mao, Z. Sun, C. Huang, G. Jia, and A. Ding, "Electromagnetic characteristics analysis of a novel ironless double-sided halbach permanent magnet synchronous linear motor for electromagnetic launch considering longitudinal end effect," *IEEE Transactions on Transportation Electrification*, vol. 10, no. 3, pp. 7467-7477, Sept. 2024.

[14] Y. Wen, G. Li, Q. Wang, X. Guo, and W. Cao, "Modeling and analysis of permanent magnet spherical motors by a multitask gaussian process method and finite element method for output torque," *IEEE Transactions on Industrial Electronics*, vol. 68, no. 9, pp. 8540-8549, Sept. 2021.

[15] Y. -H. Lin and L. Chang, "An online transfer learning framework for time-varying distribution data prediction," *IEEE Transactions on Industrial Electronics*, vol. 69, no. 6, pp. 6278-6287, June 2022.

[16] Z. Wang, X. He, B. Yang, and N. Li, "Subdomain adaptation transfer learning network for fault diagnosis of roller bearings," *IEEE Transactions on Industrial Electronics*, vol. 69, no. 8, pp. 8430-8439, Aug. 2022.

[17] R. Liu, H. Han, J. Zhang, G. Sun, and S. Lin, "3-D analytical model of magnetic field for axial-flux permanent magnet couplings," *IEEE Transactions on Magnetics*, vol. 60, no. 10, pp. 1-7, Oct. 2024, Art no. 8000707.

[18] M. Amirkhani, M. A. J. Kondelaji, A. Ghaffarpour, M. Mirsalim, and S. Vaez-Zadeh, "Study of boosted toothed biased flux permanent magnet motors," *IEEE Transactions on Transportation Electrification*, vol. 8, no. 2, pp. 2549-2564, June 2022.

[19] T. Wu, *et al.*, "Multiobjective optimization of a tubular coreless LPMSM based on adaptive multiobjective black hole algorithm," *IEEE Transactions on Industrial Electronics*, vol. 67, no. 5, pp. 3901–3910, 2019.

[20] S. M. Nabavinejad and S. Reda, "BayesTuner: leveraging Bayesian optimization for DNN inference configuration selection," *IEEE Computer Architecture Letters*, vol. 20, no. 2, pp. 166-170, 1 July-Dec. 2021.

Tao Wu (Senior Member, IEEE), received the B.E. degree and the M.S. degree from China University of Geoscience, Hubei, China, in 2001 and 2004, respectively; and the Ph.D. degree in motors and electrical appliances from Huazhong University of Science and Technology, Wuhan, China, in 2010.

He is currently an Associate Professor at the School of Automation, China University of Geoscience, Hubei, China. His current research interests include motors and controls, design and optimization of electrical drive systems.

Gang Xue, received the B.E. degree from China University of Geoscience, Hubei, China, in 2023.

He is currently a master's student at the School of Automation, China University of Geoscience, Hubei, China. His current research interests include motors and controls.

Gang Lei (Senior Member, IEEE), received the B.S. degree in mathematics from Huanggang Normal University, China, in 2003, the M.S. degree in mathematics and the Ph.D. degree in electrical engineering from Huazhong University of Science and Technology, China, in 2006 and 2009, respectively.

He is currently an Associate Professor at the University of Technology Sydney, NSW, Australia. His current research interests include design optimization of electromagnetic devices and systems.

Youguang Guo (Senior Member, IEEE), received the B.E. degree from Huazhong University of Science and Technology (HUST), China in 1985, the M.E. degree from Zhejiang University, China in 1988, and the Ph.D. degree from the University of Technology Sydney (UTS), Australia, in 2004, all in electrical engineering.

He is currently a Professor at the School of Electrical and Data Engineering, UTS. His research fields include measurement and modeling of magnetic properties of magnetic materials, electrical machine design and optimization, electric motor drives and control.

Jianguo Zhu (Senior Member, IEEE), received the B.E. degree from Jiangsu Institute of Technology, China, in 1982, the M.E. degree from Shanghai University of Technology, China, in 1987, and the Ph.D. degree from the University of Technology, Sydney, NSW, Australia, in 1995, all in electrical

engineering.

He is currently a Professor of Electrical Engineering at The University of Sydney, Australia.

His current research interests include electromagnetics, magnetic properties of materials, and electrical machines.